Scientific Research Publishing

World Journal of Mechanics, 2025, 15(3), 45-52
https://www.scirp.org/journal/wjm
ISSN Online: 2160-0503
ISSN Print: 2160-049X

Numerical Study of Flow around a Rotating Disk with Different Radius

Hiroyuki Furukawa, Yusuke Nakatani

Department of Mechanical Engineering, Meijo University, Nagoya, Japan
Email: furukawa@meijo-u.ac.jp

How to cite this paper: Furukawa, H. and Nakatani, Y. (2025) Numerical Study of Flow around a Rotating Disk with Different Radius. *World Journal of Mechanics*, **15**, 45-52.
https://doi.org/10.4236/wjm.2025.153003

Received: March 5, 2025
Accepted: March 28, 2025
Published: March 31, 2025

Copyright © 2025 by author(s) and Scientific Research Publishing Inc.
This work is licensed under the Creative Commons Attribution International License (CC BY 4.0).
http://creativecommons.org/licenses/by/4.0/

Open Access

Abstract

The flow induced by a rotating object in a vessel can be seen in fluid machinery such as centrifugal pumps and water turbines. This research focuses on the flow induced by rotating objects, especially the flow around the disk rotor in the vessel, and visualization experiments are being conducted. The following results were obtained by comparing the respective flow fields at different Reynolds numbers in a 3D visualization using Q-value. At $r = 117$ mm, when the vortex was well developed, two vortices were observed at both Reynolds numbers, although their visibility varied depending on the turbulence of the vortex. On the other hand, at $r = 127$ mm, two to four vortices were observed between Re = 3000 and 20,000. As the radius increases, the gap distance necessarily decreases. Therefore, the velocity gradient becomes larger. As the velocity gradient increases, turbulence is more likely to occur, and therefore, a variety of vortex structures may appear as in the case of $r = 127$ mm. It was found that the number of vortices may differ from region to region, as in the results for $r = 127$ and Re = 6000.

Keywords

Rotating Disk, Influence of Radius, CFD

1. Introduction

Flows around a rotating body and swirling flows around a stationary body give simple but important phenomena including Kármán flow, Bödewadt flow and Taylor vortex flow, and they have engaged historical interests in theoretical, experimental and numerical studies. The cylindrical rotor-stator cavity flow is the flow between a rotating disk and a stationary disk enclosed by an outer casing, and it presents one of the three-dimensional cross flow models [1] [2]. The rotation of the disk makes an Ekman layer on the rotating disk and a Bödewadt layer

on the stationary disk. With an increase of the rotation rate of the disk, various flow patterns appear [3], and the development of the flow has been investigated by experimental [4] and theoretical [5] approaches. In case of a narrow interdisk gap [6], the first instability of circular waves appears in the boundary layers on the rotating and the stationary disks, and the secondary instability of the spiral rolls emerges via Hopf bifurcation. Then, the solitary waves and the flows including turbulent spots appear. When the interdisk gap is wide, the boundary layers are separated and the basic flow has a core region. In this flow, transitions appear through circular rolls, spiral rolls and wavy turbulence [7]-[9]. Two types of instabilities appear: type I instability based on the inflection of the velocity profile, which initializes spiral rolls at higher rotation rate, and type II instability concerned with the Coriolis force and viscous force, which promotes circular waves and spiral rolls at lower rotation rate [10]. When the interdisk gap is very wide and it is comparable with the radii of the rotating and stationary disks, the axial flow becomes dominant and the vortex breakdown phenomena may emerge [11].

The flow induced by a rotating object in a vessel can be seen in fluid machinery such as centrifugal pumps and water turbines. The impeller plate and the upper and lower walls of the vessel can be approximated as a rotating disk and a fixed disk, and this is a field that has been studied by many researchers. This research focuses on the flow induced by rotating objects, especially the flow around the disk rotor in the vessel, and visualization experiments are being conducted. 3D calculations are performed, and the goal is to analyze the flow when it is sufficiently developed, and to visualize and compare the flow at two different radii.

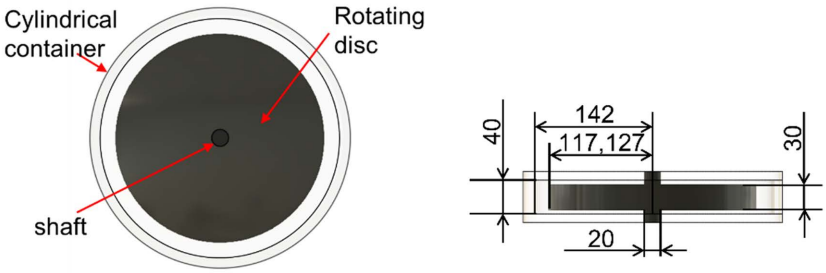

Figure 1. Analysis target.

2. Analysis Target

The flow field analyzed in this experiment is that of a rotating disk driven by a shaft in a stationary cylindrical vessel. **Figure 1** shows a schematic diagram of the analysis target. The cylindrical vessel containing the test fluid consists of two fixed disks (top and bottom) and a cylindrical frame with an inner diameter of 142.0 mm and a thickness of 40.0 mm sandwiched between them. The dimensions of the rotating disks installed inside the vessel are 117 mm and 127 mm in radius and 30.0 mm in thickness. These radius values were chosen to match the experimental studies currently in progress, and we have experimentally confirmed that the flow regime changes with the radius. The disks are mounted on a rotating shaft

with a shaft diameter of 20.0 mm. In the flow pattern between the rotating and fixed disks, the flow between the two disks, the disk fastening is 20.0 mm in diameter, the same as the axis of rotation, to make the space in the vessel symmetrical across the rotating disk.

The three analytical conditions in this experiment are the number of lattices, the Reynolds number, and the time step width. The number of lattices is 265 in the radial direction, 338 in the circumferential direction, and 81 in the axial direction of the cylindrical vessel, for a total of 7,255,170 lattices, and the Reynolds number is from 3000 to 20,000 in increments of 1000. The time increment range shall be 0.001 seconds.

3. Calculation and Visualization Methods

3.1. Governing Equation

The governing equations are the unsteady incompressible Navier-Stokes equation with cylindrical coordinates (r, θ, z) (Equation (1)) and the equation of continuity (Equation (2)).

$$\frac{\partial u}{\partial t}+\left(u\cdot\nabla\right)u=-\nabla p+\frac{1}{\mathrm{Re}}\nabla^2 u \tag{1}$$

$$\nabla\cdot u=0 \tag{2}$$

Here, u is a velocity vector with the components of (u, v, w), t is a dimensionless time based on a representative time, and p is the pressure. The discretization of the governing equations is based on the MAC method. For time integration, Euler's explicit method is used. For space integration, the QUICK method is used for the convection terms, and the secondary central difference method is used for other terms. As an initial condition, the velocity is set to 0 in all regions. As boundary conditions, the no-slip condition at each cylinder wall is applied for the velocity, and the Neumann condition based on the equation of motion is applied for the pressure. Staggered grids are used as calculation grids and are assumed to have regular intervals in each direction. The number of the grid points in the radial direction is 41, and one in the axial direction is determined linearly according to the height of the cylinders. It was confirmed that the flow state does not change qualitatively even if the number of grids is doubled. The time step was also determined by verifying the Courant number and the diffusion number. The working fluid is assumed to be a glycerin aqueous solution.

3.2. Q-Criterion

To visualize the vortex structure in a flow, we use the Q-criterion to visualize the vortex. It is a way to define the vortex using the coincidence of the vortex region in the flow and the region where the second invariant of the velocity gradient tensor of the flow field is Q > 0. The velocity gradient tensor D_{ij} can be written using the target component S_{ij} and the non-target component Ω_{ij} as follows.

$$D_{ij}=\frac{\partial u_j}{\partial x_i}=S_{ij}+\Omega_{ij}\quad\left(i,j=1,2,3\right) \tag{3}$$

The target component is called the strain rate tensor, and the non-target component is called the vorticity tensor. Each can be written as follows.

$$S_{ij} = \frac{1}{2}\left(D_{ij} + D_{ji}\right) \tag{4}$$

$$\Omega_{ij} = \frac{1}{2}\left(D_{ij} - D_{ji}\right) \tag{5}$$

The second invariant of the velocity gradient tensor, called the Q-criterion, can be written using S_{ij} and Ω_{ij} as follows.

$$Q = \frac{1}{2}\left(\Omega_{ij}\Omega_{ij} - S_{ij}S_{ij}\right) \tag{6}$$

Expanding the above equation in the cylindrical coordinate system (r, t, z) yields the following.

$$Q = -\frac{1}{2}\left\{\left(\frac{\partial u}{\partial r}\right)^2 + \left(\frac{1}{r}\frac{\partial v}{\partial \theta} + \frac{u}{r}\right)^2 + \left(\frac{\partial w}{\partial z}\right)^2\right\}$$
$$-\frac{\partial}{\partial r}\left(\frac{v}{r}\right)\frac{\partial u}{\partial \theta} - \frac{\partial w}{\partial r}\frac{\partial u}{\partial z} - \frac{1}{r}\frac{\partial w}{\partial \theta}\frac{\partial v}{\partial z} \tag{7}$$

From this equation, for Q > 0, we can define a region where the rotational motion is greater than the flow strain, which describes the vortex region.

4. Results

The results of Q-values at 100 s for Reynolds numbers 6000 and 9000 at 117 mm radius, and for Reynolds numbers 6000 and 9000 at 127 mm radius are shown.

4.1. Vortex Structures

There are four main representative vortex structures that appear in the top view. They are shown on Figure 2. The left figure is Ring-like vortex. The figure on the right is Bead-like vortex consisting of a series of spherical or elliptical vortices in the shape of beads.

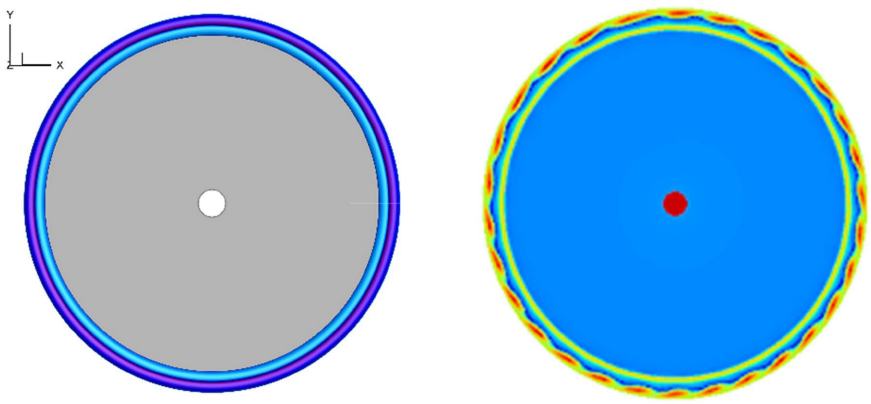

Figure 2. Vortex structures in top view.

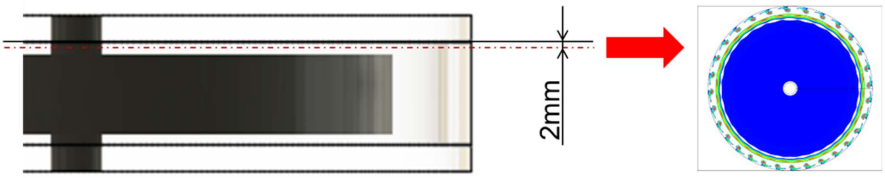

Figure 3. Measurement section used in top view.

4.2. Measurement Section Used in Top View

The top view shows a cross-section of 2 mm from the top inside the vessel as shown in Figure 3. Previous studies have shown that this cross-section is the most likely to exhibit flow characteristics.

4.3. Visualization at r = 117 (mm), Re = 6000, t = 100 (s)

Figure 4 shows a visualization of the Q-value at 117 mm radius, Reynolds number 6000, and 100 s. For the top view, two layers of Ring-like vortices are formed. For the side view, two upper and lower target vortices are formed.

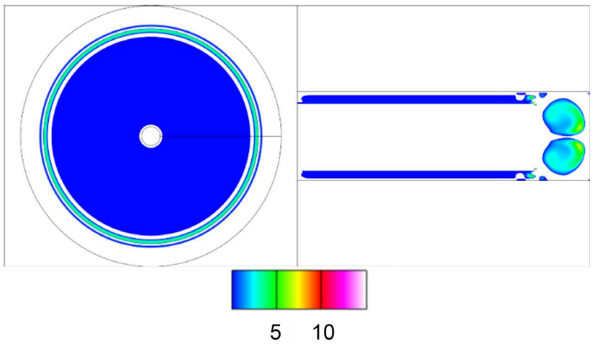

Figure 4. Visualization at r = 117 (mm), Re = 6000, t = 100 (s).

4.4. Visualization at r = 117 (mm), Re = 9000, t = 100 (s)

Figure 5 shows a visualization of the Q-value at 117 mm radius, 9000 Reynolds number, and 100 seconds. In the top view, long, stretched-looking Bead-like vortex can be observed, with elliptical vortices scattered irregularly on the outside. In the side view, the symmetry is broken, but a coherent vortex shape can be seen.

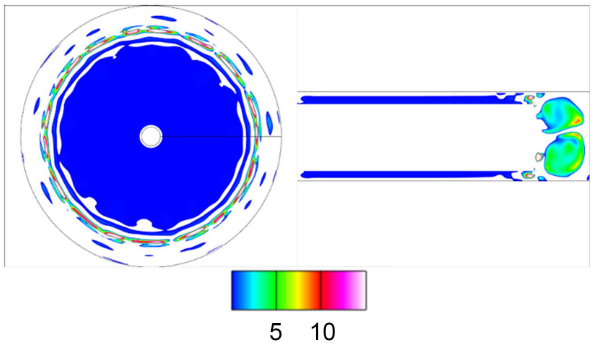

Figure 5. Visualization at r = 117 (mm), Re = 9000, t = 100 (s).

4.5. Visualization at r = 127 (mm), Re = 6000, t = 100 (s)

Figure 6 shows a visualization of the Q-value at 127 mm radius, Reynolds number 6000, and 100 seconds. A special vortex structure was observed under these conditions. In the top view, one stable Ring-like vortex was observed. In the side view, different numbers of vortices were observed in different areas. Four vortices were observed in reference section (a) and the surrounding area. The top two vortices are rounded and the bottom two are elliptical. The red region is biased toward the outside of the vessel. Three vortices were identified in and around the cross section (b) at 120˚ from the reference cross section (a). The top and middle vortices are identical to (a). In the section (c) at 264˚ from (a) and its vicinity, three vortices and one vortex that seems to have failed to form were observed. The lowest vortex has a collapsed shape. The top two vortices are almost the same shape as (a) and (b).

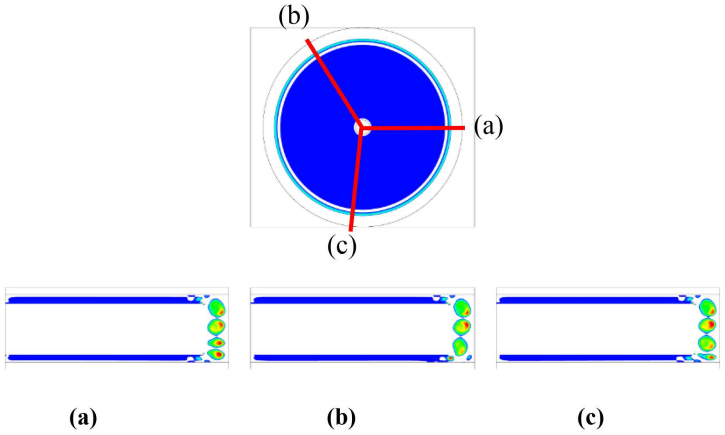

Figure 6. Visualization at r = 127 (mm), Re = 6000, t = 100 (s).

4.6. Visualization at r = 127 (mm), Re = 9000, t = 100 (s)

Figure 7 shows a visualization of the Q-value at 127 mm radius, 9000 Reynolds number, and 100 seconds. In the top view, Bead-like vortex with a series of tail-like vortices was observed on the outside, and a vortex transitioning from Ring-like vortex to Bead-like vortex was observed on the inside. In the side view, a collapsed vortex with a top and bottom target was observed.

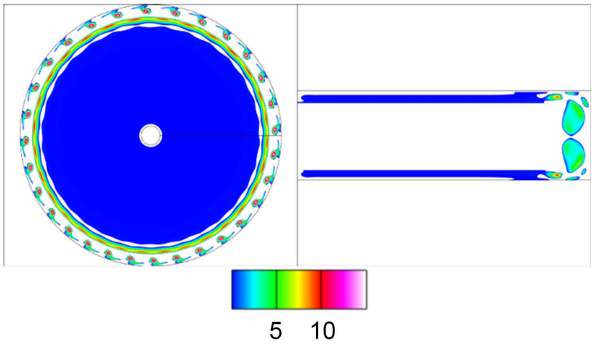

Figure 7. Visualization at r = 127 (mm), Re = 9000, t = 100 (s).

5. Conclusion

The following results were obtained by comparing the respective flow fields at different Reynolds numbers in a 3D visualization using Q-value. At r = 117 mm, when the vortex was well developed, two vortices were observed at both Reynolds numbers, although their visibility varied depending on the turbulence of the vortex. On the other hand, at r = 127 mm, two to four vortices were observed between Re = 3000 and 20,000. As the radius increases, the gap distance necessarily decreases. Therefore, the velocity gradient becomes larger. As the velocity gradient increases, turbulence is more likely to occur, and therefore, a variety of vortex structures may appear as in the case of r = 127 mm. It was found that the number of vortices may differ from region to region, as in the results for r = 127 and Re = 6000. The numerical results obtained in this study are qualitatively consistent with the results of our ongoing experimental study, which we plan to publish in a future paper.

Acknowledgements

This research was supported by a research grant from the Nitto Foundation. We would like to show our gratitude to members in our laboratory for sharing their pearls of wisdom with us during this research.

Conflicts of Interest

The authors declare no conflicts of interest regarding the publication of this paper.

References

[1] Launder, B., Poncet, S. and Serre, E. (2010) Laminar, Transitional, and Turbulent Flows in Rotor-Stator Cavities. *Annual Review of Fluid Mechanics*, **42**, 229-248. https://doi.org/10.1146/annurev-fluid-121108-145514

[2] Viazzo, S., Poncet, S., Serre, E., Randriamampianina, A. and Bontoux, P. (2011) High-order Large Eddy Simulations of Confined Rotor-Stator Flows. *Flow, Turbulence and Combustion*, **88**, 63-75. https://doi.org/10.1007/s10494-011-9345-0

[3] Schouveiler, L., Le Gal, P. and Chauve, M.P. (2001) Instabilities of the Flow between a Rotating and a Stationary Disk. *Journal of Fluid Mechanics*, **443**, 329-350. https://doi.org/10.1017/s0022112001005328

[4] Savaş, Ö. (1987) Stability of Bödewadt Flow. *Journal of Fluid Mechanics*, **183**, 77-94. https://doi.org/10.1017/s0022112087002532

[5] Tuliska-Sznitko, E., Serre, E. and Bontoux, P. (2002) On the Nature of the Boundary Layers Instabilities in a Flow between a Rotating and a Stationary Disc. Comptes Rendus. *Mécanique*, **330**, 91-99. https://doi.org/10.1016/s1631-0721(02)01432-8

[6] Cros, A. and Le Gal, P. (2002) Spatiotemporal Intermittency in the Torsional Couette Flow between a Rotating and a Stationary Disk. *Physics of Fluids*, **14**, 3755-3765. https://doi.org/10.1063/1.1508796

[7] Schouveiler, L., Le Gal, P., Chauve, M.P. and Takeda, Y. (1999) Spiral and Circular Waves in the Flow between a Rotating and a Stationary Disk. *Experiments in Fluids*, **26**, 179-187. https://doi.org/10.1007/s003480050278

[8] Cros, A., Floriani, E., Le Gal, P. and Lima, R. (2005) Transition to Turbulence of the

Batchelor Flow in a Rotor/stator Device. *European Journal of Mechanics*, **24**, 409-424. https://doi.org/10.1016/j.euromechflu.2004.11.002

[9] Lopez, J.M., Marques, F., Rubio, A.M. and Avila, M. (2009) Crossflow Instability of Finite Bödewadt Flows: Transients and Spiral Waves. *Physics of Fluids*, **21**, Article 114107. https://doi.org/10.1063/1.3262817

[10] Poncet, S., Serre, É. and Le Gal, P. (2009) Revisiting the Two First Instabilities of the Flow in an Annular Rotor-Stator Cavity. *Physics of Fluids*, **21**, Article 064106. https://doi.org/10.1063/1.3156859

[11] Spohn, A., Mory, M. and Hopfinger, E.J. (1998) Experiments on Vortex Breakdown in a Confined Flow Generated by a Rotating Disc. *Journal of Fluid Mechanics*, **370**, 73-99. https://doi.org/10.1017/s0022112098002092